REPORT DOCUMENTATION PAGE

Form Approved
OMB NO. 0704-0188

Public reporting burden for this collection of information is estimated to average 1 hour per response, including the time for reviewing instructions, searching existing data sources, gathering and maintaining the data needed, and completing and reviewing the collection of information. Send comment regarding this burden estimates or any other aspect of this collection of information, including suggestions for reducing this burden, to Washington Headquarters Services, Directorate for information Operations and Reports, 1215 Jefferson Davis Highway, Suite 1204, Arlington, VA 22202-4302, and to the Office of Management and Budget, Paperwork Reduction Project (0704-0188), Washington, DC 20503.

1. AGENCY USE ONLY *(Leave blank)*	2. REPORT DATE	3. REPORT TYPE AND DATES COVERED
		Reprint

4. TITLE AND SUBTITLE

TITLE ON REPRINT

5. FUNDING NUMBERS

DAAD19-99-1-0132

6. AUTHOR(S)

AUTHOR(S) ON REPRINT

7. PERFORMING ORGANIZATION NAMES(S) AND ADDRESS(ES)

Duke University

8. PERFORMING ORGANIZATION REPORT NUMBER

9. SPONSORING / MONITORING AGENCY NAME(S) AND ADDRESS(ES)

U.S. Army Research Office
P.O. Box 12211
Research Triangle Park, NC 27709-2211

10. SPONSORING / MONITORING AGENCY REPORT NUMBER

ARO 39804.3-CI

11. SUPPLEMENTARY NOTES

The views, opinions and/or findings contained in this report are those of the author(s) and should not be construed as an official Department of the Army position, policy or decision, unless so designated by other documentation.

12a. DISTRIBUTION / AVAILABILITY STATEMENT

Approved for public release; distribution unlimited.

12 b. DISTRIBUTION CODE

13. ABSTRACT *(Maximum 200 words)*

ABSTRACT ON REPRINT

20010413 139

14. SUBJECT TERMS			15. NUMBER IF PAGES
			16. PRICE CODE
17. SECURITY CLASSIFICATION OR REPORT	18. SECURITY CLASSIFICATION OF THIS PAGE	19. SECURITY CLASSIFICATION OF ABSTRACT	20. LIMITATION OF ABSTRACT
UNCLASSIFIED	UNCLASSIFIED	UNCLASSIFIED	UL

WAVE PROPAGATION IN PHOTONIC CRYSTAL MODELS

S. VENAKIDES
Dept. of Mathematics, Box 90320, Duke University, Durham, NC 27708-0320, USA
E-mail: ven@math.duke.edu

M. A. HAIDER
Dept. of Mathematics, Box 8205, North Carolina State University, Raleigh, NC 27695-8205, USA
E-mail: mahaider@math.ncsu.edu

V. PAPANICOLAOU
Dept. of Mathematics and Statistics, Wichita State University. Wichita, KS 67260-0033, USA and Dept. of Mathematics, National Technical University - Athens, Athens 157 80 (Zografou), GREECE
E-mail: vpapan@softlab.ece.ntua.gr

We compute the transmission properties of 2-D electromagnetic TM waves that are normally incident on a Fabry-Perot structure with mirrors consisting of photonic crystals. We use a boundary integral formulation with quadratic boundary elements and utilize the Ewald representation for the Green's functions. We trace the frequencies of the Fabry-Perot cavity modes traversing the photonic bandgap as the cavity length increases and calculate corresponding Q-values. For the case of lossy dielectrics, we compare bandgap frequencies and Q-values to experimental results obtained by H. Everitt and his group at Duke University.

1 Introduction

We model the scattering of electromagnetic waves in 2-D photonic crystal lattices consisting of one dielectric material embedded in another in a configuration which is spatially periodic in the X and Y directions and homogeneous in the Z direction. For these structures, the lattice geometry, dielectric contrast and dielectric loss properties of a photonic crystal all influence the manner in which electromagnetic waves propagate through the crystal. It is well known that 2-D crystals exhibit *photonic bandgaps*, that is, intervals in their frequency spectrum over which there are no waves propagating through the lattice (e.g. Joannopoulos et al.[5], Yablonovitch[13]). Localized *defect modes* can appear as resonant peaks at bandgap frequencies when local physical defects are introduced into the 2-D infinite lattice.

In practice, photonic crystals have finite extent which plays a central role in the design of optical and electronic devices including filters, lasers

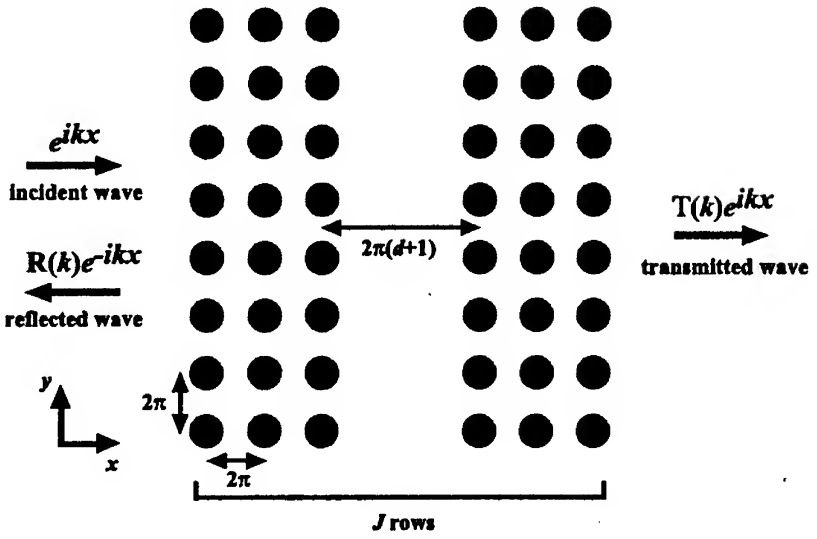

Figure 1. Fabry-Perot Structure with Photonic Crystal Mirrors.

and microwave antennas. Quantitative characterizations of transmission near resonant frequencies are needed for optimal design of practical devices. For example, the efficiency of a laser cavity (built as a defect in a photonic crystal) increases as the transmission peak at the resonance becomes sharper.

We consider finite extent by truncating the infinite 2-D periodic lattice in the X direction so that the dielectric permittivity is constant outside a certain interval in X and we model the scattering of plane electromagnetic waves. We employ a boundary integral formulation which reduces the problem from 2-D to 1-D and also enforces, automatically, radiation conditions through the choice of appropriate Green's functions. The Ewald[4] representation of the Green's function is used to ensure rapid convergence and a further simple reduction is applied to facilitate numerical evaluation. Our formulation is valid for both lossless and lossy dielectrics, for waves incident at an arbitrary angle and is flexible with respect to the geometry of the dielectric configuration. It is described in detail in a recent paper.[12]

In this study, we model an experimental setup of H. Everitt and his group in the Physics Department at Duke University. We analyze the transmission properties of a plane transverse magnetic (TM) wave that is normally incident on the geometry of Figure 1 ($J = 6$ in the figure). The geometry consists of

two square lattices of parallel circular rods, truncated in the X direction, that are separated by a Fabry-Perot cavity of length $d > 0$. In particular, we characterize defect modes that are of central interest to the experimental work in the case of both lossless and lossy dielectric rods. Although we limit the present study to circular rods and normal incidence, our approach is applicable to a wide variety of 2-D geometries with periodicity in the Y direction.

2 Governing Equations

2.1 Maxwell's Equations

For a time-periodic electric field $\mathbf{E}(\mathbf{R})e^{-i\omega t}$ and a time-periodic magnetic field $\mathbf{H}(\mathbf{R})e^{-i\omega t}$, the governing equations in both the interior and exterior of the dielectric rods are Maxwell's equations:

$$\nabla \times \mathbf{E}(\mathbf{R}) = \frac{i\omega}{c}\mathbf{H}(\mathbf{R}), \quad \nabla \times \mathbf{H}(\mathbf{R}) = -\frac{i\omega}{c}\epsilon(\mathbf{R})\mathbf{E}(\mathbf{R}) \tag{1}$$

$$\nabla \cdot \mathbf{H} = 0, \qquad \nabla \cdot \mathbf{E} = 0 \tag{2}$$

where $\mathbf{R} = (X, Y)$, c is the speed of light and ϵ is the relative dielectric permittivity of the medium. In the case of *E polarization* (transverse magnetic or TM waves), $\mathbf{E} = (0, 0, \psi)$ and $\mathbf{H} = (H_1, H_2, 0)$ and Maxwell's equations can be reduced to the Helmholtz equation for ψ:

$$\left(\partial_X^2 + \partial_Y^2\right)\psi + \frac{\omega^2}{c^2}\epsilon(X, Y)\psi = 0 \tag{3}$$

where the permittivity $\epsilon(X, Y)$ is periodic in the variable Y. In addition to this equation, we have *matching conditions* on the rod surfaces (dielectric interfaces) which require continuity of ψ and $\nabla\psi$. In considering (3), the following conditions apply:

- The field ψ in the exterior is the sum of an incident plane wave $\psi_{in}(X, Y)$ and a scattered wave $\psi_{sc}(X, Y)$, that satisfies (3) plus a radiation condition at $x = \pm\infty$.

- On the *interface* of each rod, the following matching conditions are satisfied:

$$\psi = \psi_{in} + \psi_{sc} = \psi_{int}, \qquad \partial_n\psi = \partial_n\psi_{in} + \partial_n\psi_{sc} = \partial_n\psi_{int} \tag{4}$$

2.2 *Nondimensionalization*

We assume a Y-periodic geometry of period a and plane wave incident radiation of frequency f. We introduce the nondimensional space variables $x = 2\pi X/a, y = 2\pi Y/a$ and the reduced frequency $k = fa/c = \omega a/(2\pi c)$. In the new variables, the Helmholtz equation for the field ψ is:

$$\left(\partial_x^2 + \partial_y^2\right)\psi + k^2\epsilon(x,y)\psi = 0 \tag{5}$$

where we have retained the symbol ψ for the field and the permittivity function $\epsilon(x,y)$ is 2π-periodic in the variable y. In this paper, we assume that the exterior dielectric permittivity is unity, so that:

$$\epsilon(x,y) = \begin{cases} 1 & \text{outside the rods} \\ \varepsilon_j > 1 & \text{inside the } j\text{-th rod} \end{cases} \tag{6}$$

The quantity ε_j is thus the dielectric contrast $\varepsilon_j = \epsilon_{int}/\epsilon_{ext}$ of the jth rod. For this study, we restrict our analysis to normally incident fields which have the form:

$$\psi_{in}(x,y) = e^{ikx} \tag{7}$$

We allow for the consideration of both *lossless* materials (k real) and *lossy* materials in which k can have a small positive imaginary part. We require that the scattered field ψ_{sc} also satisfy the pseudo-periodic condition:

$$\psi_{sc}(x, y+2\pi) = \psi_{sc}(x,y) \tag{8}$$

As a consequence of this periodicity, we can restrict our attention to a single interval of length 2π in the y-direction.

3 Boundary Integral Equations and Green's Functions

3.1 *The System of Integral Equations on the Boundary*

We denote the jth dielectric interface by ∂D_j and the union of all interfaces by $\partial D = \cup_{j=1}^{J} \partial D_j$. The governing equation (3) can be reduced to the following system of integral equations on the boundary which must be satisfied for each $\hat{\mathbf{r}} \in \partial D$:[12]

$$\frac{1}{2}\psi_{sc}(\hat{\mathbf{r}}) - \int_{\partial D} \frac{\partial G(\hat{\mathbf{r}} - \mathbf{r})}{\partial n(\mathbf{r})} + \int_{\partial D} G(\hat{\mathbf{r}} - \mathbf{r})\partial_n \psi_{sc}(\mathbf{r}) ds(\mathbf{r}) = 0 \tag{9}$$

$$\frac{1}{2}\psi_{sc}(\hat{\mathbf{r}}) + \int_{\partial D_j} \frac{\partial \Phi_j(\hat{\mathbf{r}} - \mathbf{r})}{\partial n(\mathbf{r})}\psi_{sc}(\mathbf{r}) ds(\mathbf{r}) - \int_{\partial D_j} \Phi_j(\hat{\mathbf{r}} - \mathbf{r})\partial_n \psi_{sc}(\mathbf{r}) ds(\mathbf{r}) = W(\hat{\mathbf{r}}) \tag{10}$$

$$W(\hat{\mathbf{r}}) = -\frac{1}{2}\psi_{in}(\hat{\mathbf{r}}) - \int_{\partial D_j} \frac{\partial \Phi_j(\hat{\mathbf{r}}-\mathbf{r})}{\partial n(\mathbf{r})}\psi_{in}(\mathbf{r})ds(\mathbf{r}) + \int_{\partial D_j} \Phi_j(\hat{\mathbf{r}}-\mathbf{r})\partial_n\psi_{in}(\mathbf{r})ds(\mathbf{r}) \tag{11}$$

The solution of the above system of integral equations yields values of ψ_{sc} and $\partial_n\psi_{sc}$ on the dielectric interfaces which can then be used to calculate the scattered field at any point $\hat{\mathbf{r}}$ in the exterior domain using Green's second identity:

$$\psi_{sc}(\hat{\mathbf{r}}) = \sum_j \int_{\partial D_j} \left(-G(\hat{\mathbf{r}}-\mathbf{r})\partial_n\psi_{sc}(\mathbf{r}) + \frac{\partial G(\hat{\mathbf{r}}-\mathbf{r})}{\partial n(\mathbf{r})}\psi_{sc}(\mathbf{r}) \right) ds(\mathbf{r}) \tag{12}$$

The above system of integral equations is of Fredholm first kind and hence not well-posed. Nevertheless, the logarithmic kernel allows for accurate numerical inversion at the lower incident frequencies and aspect ratios considered in the present study. In current work, we are recasting the system into one of Fredholm second kind to simulate higher frequencies and aspect ratios.

3.2 Green's Functions

The field at the point $\mathbf{r} = (x, y)$ produced by a radiating y-periodic monopole of the equation (3) located at the point $\hat{\mathbf{r}} = (\hat{x}, \hat{y})$ is given by the following Fourier form:

$$G(\mathbf{r}-\hat{\mathbf{r}}; k^2) = \frac{1}{4\pi} \sum_{m=-\infty}^{\infty} \frac{e^{-\sqrt{-\lambda_m}|x-\hat{x}|}}{\sqrt{-\lambda_m}} e^{im(y-\hat{y})} \tag{13}$$

where $\lambda_m = k^2 - m^2$, with $\Re\{\sqrt{-\lambda_m}\} \geq 0$ (if $\Re\{\sqrt{-\lambda_m}\} = 0$, we take $\Im\{\sqrt{-\lambda_m}\} \leq 0$). These inequalities guarantee proper growth and radiation conditions in the x-direction. This expression for the Green's function is valid when the parameter values are such that the denominator in (13) is nonzero for every m. Since (13) is a slowly converging series when $|x - \hat{x}| \ll 1$, Ewald's method[6] is used to re-write the Green's function in a form that is rapidly converging. Via a Taylor expansion in the remaining integral of Ewald's formula, we obtain a representation of the Green's function entirely in terms of special functions that can be easily evaluated numerically:[12]

$$G(\mathbf{r}-\hat{\mathbf{r}}; k^2) = \frac{1}{4} \sum_{m=-\infty}^{\infty} \sum_{n=0}^{\infty} \frac{(Ek)^{2n}}{\pi n!} E_{n+1}\left(\frac{R_m^2}{4E^2}\right)$$
$$+ \frac{1}{8\pi} \sum_{m=-\infty}^{\infty} \frac{e^{im(y-\hat{y})}}{\sqrt{-\lambda_m}} \left[e^{(x-\hat{x})\sqrt{-\lambda_m}} \operatorname{erfc}\left(E\sqrt{-\lambda_m} + \frac{(x-\hat{x})}{2E} \right) \right.$$

$$+ e^{-(x-\hat{x})\sqrt{-\lambda_m}}\mathrm{erfc}\left(E\sqrt{-\lambda_m} - \frac{(x-\hat{x})}{2E}\right)\Bigg] \qquad (14)$$

In (14), $E_n(z)$ is the exponential integral function[1] of degree n, $R_m^2 = (x - \hat{x})^2 + (y - \hat{y} + 2\pi m)^2$ and E is an arbitrary real number. The choice $E = 1/|k|$ provides an appropriate balance between the singular and regular parts of the Ewald representation[12]. In the interior of each rod, we use the free space radiating Green's function of the Helmholtz equation:

$$\Phi_j(\mathbf{r} - \hat{\mathbf{r}}) = \frac{i}{4} H_0^{(1)}(k_j|\mathbf{r} - \hat{\mathbf{r}}|) \qquad (15)$$

where $H_0^{(1)} = J_0 + iY_0$ is the zero-order Hankel function of the first kind and $k_j = k\sqrt{\epsilon_j}$.

4 Numerical Solution of the Boundary Integral Equations

For a lattice period consisting of J circular rods, a computational mesh is required on the union $\partial D = \bigcup_{j=1}^{J} \partial D_j$ of dielectric interfaces. We utilize 3-node quadratic *boundary elements* and each rod interface is partitioned into M identical boundary elements. We denote the unknowns $\psi_{sc}, \partial_n \psi_{sc}$ on the mth element of the jth rod by $\psi_m^j, \partial_n \psi_m^j$. Within each boundary element, a local coordinate s ($s \in [-1, 1]$) is introduced and the rod surface, the unknown fields and the incident wave in (9)-(11) are all approximated in terms of three nodal values via the following quadratic interpolations:

$$\mathbf{r}_m^j(s) = \sum_{\tau=1}^{3} (\mathbf{r}_m^j)_\tau N_\tau(s) \qquad (16)$$

$$\psi_m^j(s) = \sum_{\tau=1}^{3} (\psi_m^j)_\tau N_\tau(s), \quad \partial_n \psi_m^j(s) = \sum_{\tau=1}^{3} (\partial_n \psi_m^j)_\tau N_\tau(s) \qquad (17)$$

The nodal values of the unknowns are given by $(\psi_m^j)_\tau = \psi_m^j(\tau - 2)$, $(\partial_n \psi_m^j)_\tau = \partial_n \psi_m^j(\tau - 2)$ and the quadratic basis is:

$$\{N_1(s), N_2(s), N_3(s)\} = \frac{1}{2}\{-s(1-s), 2(1-s)(1+s), s(1+s)\} \qquad (18)$$

To satisfy C^1 inter-element continuity, we move the middle node of each element to an appropriate point off the circle, the coordinates of which can be readily calculated.[12] We substitute (16)-(17) into the integral equations (9)-(10), label each mesh node with a global index p, and hence obtain a discretized system of integral equations at each mesh node $\hat{\mathbf{r}}_p$. Our procedure for the numerical solution of the discretized equations consists of evaluating all element integrals, assembling a linear algebraic system for the unknowns $\psi_p, \partial_n \psi_p$, and solving the resulting linear system.

The element integrals involve our two Green's functions G and Φ_j. In evaluating G, it is most efficient to use the Fourier form (13) when $|x-\hat{x}| > \delta$ and the modified Ewald form (14) when $|x-\hat{x}| \leq \delta$ where we find that an appropriate choice is $\delta = 0.2$. The Hankel function in Φ_j is evaluated using standard series expansions.[1] Element integrals are computed accurately using a standard low order Gaussian quadrature formula or a low order modified Gaussian quadrature formula with logarithmic weighting function[10], as appropriate. In our computations, all element integrals are evaluated using $Q = 8$ quadrature points. For more detailed information on our numerical integration procedures, the reader is referred to our recent paper.[12]

There are a total of $8MJ$ unknowns which are the real and imaginary parts of ψ_p and $\partial_n \psi_p$ at each mesh node $\hat{\mathbf{r}}_p$. Once all element integrals have been computed, a linear algebraic system can be assembled by passing from the local element indices j, m, τ to the global mesh index p. Since the matrix in the linear algebraic system is dense, we employ a direct solution technique: Gaussian elimination with partial pivoting. All computations were performed in C^{++} on a 233MHz PowerPC G3 processor.

5 Results

We simulate experiments that are being performed by H. Everitt and his group at Duke University and compute scattering properties for the lattice depicted in Figure 1 for the case of normally incident transverse magnetic (TM) waves. We compute the transmission amplitude $|T(k)|$ as defined in Figure 1 for reduced frequency $k < 1$ in which case there is exactly one transmitted and one reflected wave mode. All computations assume a rod radius to lattice constant ratio of 0.1524 and we consider rods in air with dielectric contrast of $\varepsilon = 12.0$ for the case of lossless and lossy dielectrics.

Figure 1 depicts a Fabry-Perot structure that involves two mirrors separated by a cavity. It is well known that, due to the presence of the cavity, transmission through the structure in the bandgap frequency region is possible close to resonant bandgap frequencies[8], as is shown in Figure 4. As the total number of rows J increases, the mirrors become more reflecting and the peaks in Figure 4 become sharper. At each resonance, a field tends to be maintained within the cavity which tends to a localized defect mode as $J \to \infty$.

We first analyze the lossless case ($\mathrm{Im}(\varepsilon_j) = 0$), starting with the transmission properties of the mirrors themselves, by setting $d = 0$ and considering a square lattice with J rows. The transmission amplitude T is shown versus frequency k for a lattice of 4 rows and a lattice of 6 rows (Fig. 2). We have found that the number of boundary elements per rod M must be increased

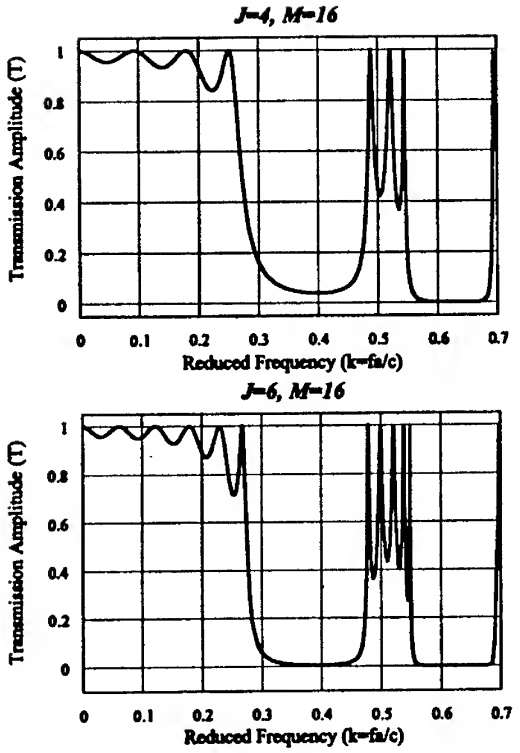

Figure 2. Photonic crystal square lattice with J rows ($d = 0$). Transmission plots are shown for the cases of $J = 4$ (top) and $J = 6$ (bottom). Computations are performed with $M = 16$ boundary elements per row.

as k increases and $M = 16$ was sufficient for the range of frequencies that are shown. Similar transmission graphs have been calculated numerically by other researchers (e.g. Bell et al.[3],Qiu et al.[7], Sigalas et al.[9]).

We see the origin of two bandgaps, roughly one between $k = 0.30$ and $k = 0.47$ and the other between $k = 0.55$ and $k = 0.68$. As we increase J, these intervals of k tend to bandgaps of the (doubly periodic) infinite lattice in which there is zero transmission. We use the term "bandgap" only in reference to transmission of normally incident waves, and not in the sense of a *complete bandgap* which would completely block transmission for all angles of incidence. Comparing our results with the atlas of complete bandgaps in Joannopoulos et al. [5], we conclude that our bandgap on the left contains a

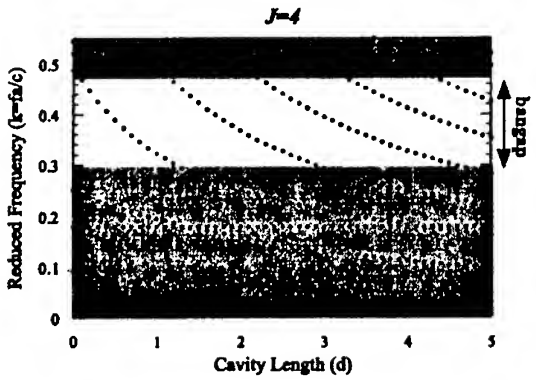

Figure 3. Fabry-Perot configuration ($d > 0$). Peak transmission frequencies are shown as functions of Fabry-Perot cavity length. The unshaded area corresponds to the first bandgap region.

complete bandgap while the one on the right does not. For our application, we locate (approximately) the left bandgap of the infinite lattice by increasing J until the frequency interval in which $T < 0.01$ is uniquely determined to two decimal places. Using this criterion, we find that the left bandgap is the interval $(0.29, 0.47)$. In the context of the finite lattice, we refer to this interval as the first bandgap. We also refer to the complement of the bandgaps for $k > 0$ as the set of *frequency bands*.

For the photonic crystal with J rows ($d = 0$), we have observed that the transmission amplitude has $J - 1$ peaks in each band (excluding the peak at $k = 0$). We can trace the location of these peaks through the first band and bandgap for increasing values of the cavity length d. An example for the case $J = 4$ is shown in Figure 3. For the range of frequencies shown, accurate numerical results could be obtained with $M = 10$ elements per row. The results clearly indicate that, as d increases, peaks move towards decreasing values of k. Each peak that leaves the second band and enters the first bandgap region turns into a Fabry-Perot resonance that traverses the bandgap as d is further increased, eventually exiting the bandgap and entering the lowest band. We have performed similar calculations for $J = 8$ in the first bandgap (Fig. 5(top)). The phenomenon of the transmission peaks traversing the bandgap persists.

The horizontal lines in Figure 3 correspond to transmission peaks of each of the mirrors ($J/2$ rows). Based on our observations, there should be $J/2 - 1$ horizontal lines in each band. Our explanation of this phenomenon is that

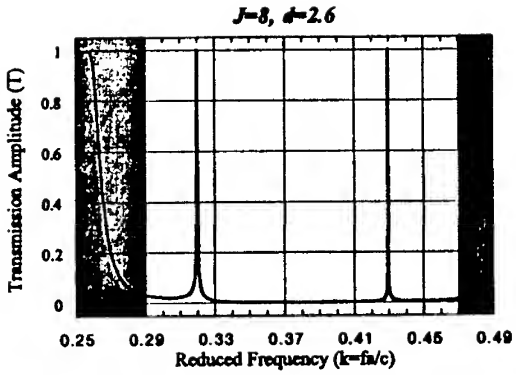

Figure 4. Fabry-Perot configuration ($d > 0$). Two Fabry-Perot resonances are shown in the first bandgap (unshaded area).

there is total transmission through each mirror at the horizontal line frequencies and, therefore, total transmission occurs through the two mirrors successively without any dependence on the cavity length d.

The sharpness of a transmission peak at bandgap frequencies is of interest since, in the case of a laser cavity, it is related to the efficiency of the laser (Fig. 4). The sharpness or "quality" of the transmission peaks is measured by the *Q-value* which is defined as $Q = k/\Delta k$ where k is the resonant frequency and $\Delta k = |k_2 - k_1|$ where $T^2(k_1) = T^2(k_2) = 1/2$ (Fig. 5(bottom)). We observe a local maximum in each Q-value as the resonance traverses the bandgap. New resonances that enter the bandgap peak at successively higher Q-values as they traverse the bandgap. When we plot Q-values versus frequency (Fig. 6), we observe that the maximum Q-values are located at resonant bandgap frequencies which are away from the endpoints of the bandgap.

The curves of Figure 5(top) are close approximations of the defect modes associated with the case $J = \infty$ of perfect mirrors. Indeed, the locations of the resonant frequencies changes minimally with increasing J. Thus, in Figures 5-6, we have labeled the resonances DM1, DM2, ..., DM5 where "DM" stands for "defect mode" in correspondence to terminology for the case $J = \infty$. Our numerical results for the locations of the Fabry-Perot resonant frequencies are in excellent agreement with the experimental data (Fig. 7). On the other hand, Q-values for these defect modes, as predicted by the lossless model, consistently overestimate their experimental counterparts. As such, it is necessary to account for dielectric loss in order to accurately quantify laser efficiency of the Fabry-Perot cavity under consideration.

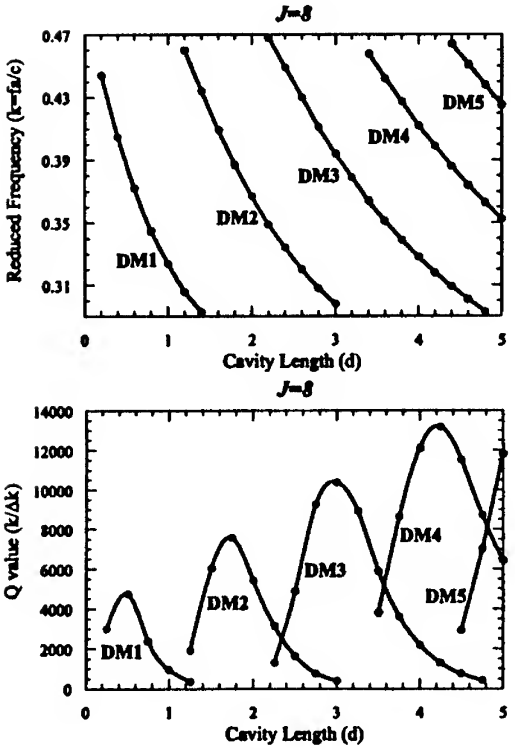

Figure 5. Fabry-Perot Configuration ($d > 0$). Fabry-Perot resonant frequencies (i.e. bandgap peak transmission frequencies) are shown as functions of the cavity length for each resonance (top). For the above resonances, Q values are shown as functions of cavity length (bottom). Dots represent computed values and curves shown are cubic spline interpolations, while DM stands for defect mode.

We introduce a small amount of loss into the dielectric rods by adding a small imaginary part $\mathrm{Im}(\varepsilon_j)$ to the exterior dielectric permittivity in the boundary integral model. Our lossy model has been compared to 2-D scattering experiments performed by H. Everitt and his group at Duke University.[2] In these experiments, the loss tangent of all the rods is identical with a value of approximately $\tan\delta = \mathrm{Im}(\varepsilon_j)/\mathrm{Re}(\varepsilon_j) \approx 0.002$. Some representative comparisons between the model and experiments are shown for a Fabry-Perot cavity with increasing mirror thickness (Fig. 8). Our simulations are in good agreement with the experimentally observed Q-values and capture the lim-

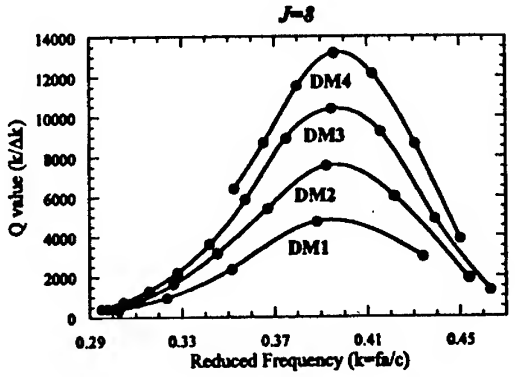

Figure 6. Fabry-Perot Configuration ($d > 0$). For the resonances of the previous figure, Q values are shown as functions of frequency. Dots represent computed values and curves shown are cubic spline interpolations.

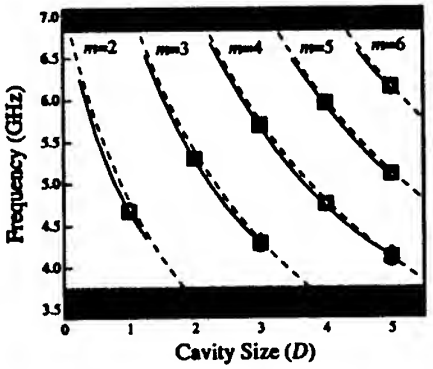

Figure 7. Measured Fabry-Perot mode frequencies as a function of cavity length for the case of square lattice mirrors with $J = 2, 3, 4$ and 5 (circles, squares, triangle and diamonds, respectively). The solid lines are predictions of the 2-D boundary integral model while the dashed lines are predictions of a 1-D layer model. The integer m is used to label the defect modes.

iting behavior with increasing mirror thickness $N = J/2$ (Fig. 8(left)). It can be observed that an accurate prediction of Q-values requires both the incorporation of loss in the dielectric rods and a genuinely 2-D model. Our model also predicts the drop in peak transmission amplitude with increasing mirror thickness that is observed in the experiment (Fig. 8(right)). The de-

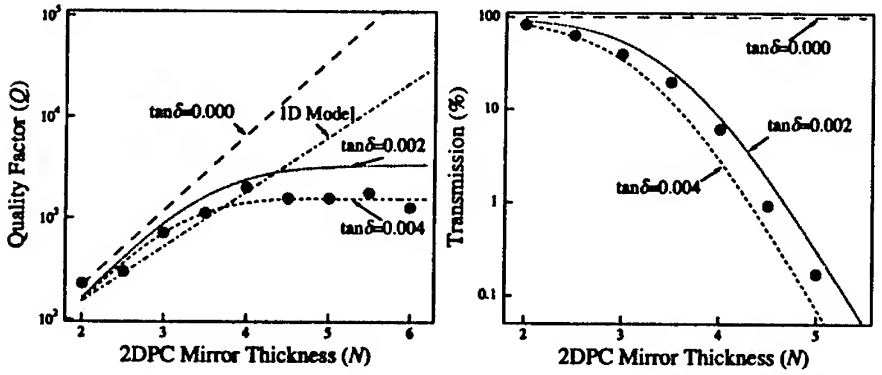

Figure 8. (left) Measured quality factors (Q-values) for the Fabry-Perot cavity plotted as a function of mirror thickness $N = J/2$ for defect mode $m = 4$ and cavity length $D = d = 3$ (filled circles). Predictions of the boundary integral model with loss ($\tan\delta = 0.002, 0.004$), without loss ($\tan\delta = 0.000$) as well as the 1-D layer model are shown. (right) Peak transmission of this mode as a function of N compared to the lossy ($\tan\delta = 0.002, 0.004$) and lossless ($\tan\delta = 0.000$) boundary integral model.

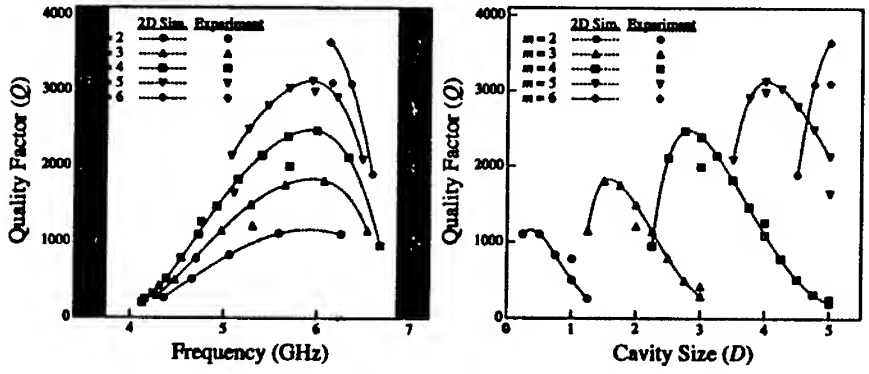

Figure 9. Quality factors (Q-values) for the 2-D Fabry-Perot cavity as a function of: (left) frequency and (right) cavity length for all modes with $J = 8(N = 4)$ from experimental measurements (filled symbols) and the 2-D boundary integral model (open symbols joined by dashed lines). The grey areas indicate frequencies outside the photonic bandgap.

fect modes predicted by our model are plotted as functions of frequency and cavity length and compared to the corresponding experimental results. (Fig. 9). It is evident from Figure 9(right) that the model is effective in associating

the experimentally observed Q-values with the various defect modes that can be sustained in the Fabry-Perot cavity.

We believe that our boundary integral model serves as a useful tool for the experimentalist in that it can quantify the location and quality of bandgaps and resonant modes for lossy dielectrics as function of lattice geometry and dielectric material parameters. This modeling approach can lead to the formulation of design rules for optimal performance of 2-D photonic crystal devices. In current work, we are extending our boundary integral model of 2-D EM scattering to take full advantage of separability in the exterior Green's function. The resulting "fast" boundary integral model will allow for the simulation of EM scattering in larger 2-D lattices with localized defects.

Acknowledgments

This work has been supported by grants ARO DAAH04-96-1-0157, ARO DAAD19-99-1-0132 and NSF DMS-9705931. We would like to thank H. Everitt, M. Beaky and U. Ozgur for valuable discussions and for making their experimental results available to us. S.V. also wishes to thank C. M. Bowden, J. P. Dowling, M. Scalora, J. Lavery and L. Katehi for helpful discussions.

References

1. M. Abramowitz and I. A. Stegun, *Handbook of mathematical functions*, (Dover, New York, 1972).
2. M.M. Beaky, J.B. Burke, H.O. Everitt, M.A. Haider and S. Venakides, *IEEE Transactions on Microwave Theory* **47**, 2085 (1999)
3. P.M. Bell, J.B. Pendry, L. Martin Moreno and A.J. Ward, *Comp. Phys. Comm.* **85**, 306 (1995).
4. P.P. Ewald, *Annalen Der Physik* **64**, 253 (1921).
5. J.D. Joannopoulos, R.D. Meade and J.N. Winn, *Photonic crystals: Molding the flow of light*, (Princeton University Press, Princeton, 1995).
6. V. Papanicolaou, *Jrnl. Comp. Anal. Appl.* **1**, 105 (1999).
7. Y. Qiu, K.M. Leung, L. Carin and D. Kralj, J. Appl. Phys. **77**, 3631 (1995).
8. M.M. Sigalas, K.M. Ho, R. Biswas and C.M. Soukoulis, Physical Review B **57**, 3815 (1998).
9. M.M. Sigalas, C.M. Soukoulis, E.N. Economou, C.T. Chan and K.M. Ho, Physical Review B **48**, 14121 (1993).
10. A.H. Stroud and D. Secrest, *Gaussian Quadrature Formulae*, (Prentice-Hall, New York, 1966).

11. J. Strain, *J. Comp. Phys.* **99**, 251 (1992).
12. S. Venakides, M.A. Haider and V. Papanicolaou, SIAM J. Appl. Math **to appear**, (2000).
13. E. Yablonovitch, J. Opt. Soc. Am. B **10**, 283 (1993).